PAPER

Advanced LIGO: length sensing and control in a dual recycled interferometric gravitational wave antenna

To cite this article: Kiwamu Izumi and Daniel Sigg 2017 *Class. Quantum Grav.* **34** 015001

Advanced LIGO: Length Sensing and Control in a Dual Recycled Interferometric Gravitational Wave Antenna

Kiwamu Izumi* and Daniel Sigg

LIGO Hanford Observatory, PO Box 159 Richland, WA 99352-0159

(Dated: October 26, 2016)

Length sensing and control is vital for Advanced LIGO and its goal of performing astrophysical searches. The current kilometer scale gravitational wave antennae are dual recycled Michelson interferometers enhanced with Fabry-Perot resonators in the arms. Observation requires the lengths of all optical cavities to be precisely servoed in the vicinity of a resonance using feedback controls. Simultaneously achieving robustness and low-noise is challenging due to cross-couplings between the multiple coupled optical resonators. We analytically derive the Advanced LIGO sensing and control scheme, calculate the effects of radiation pressure forces and review the current strategies of minimizing the coupling of noise into the gravitational wave readout.

* izumi_k@ligo-wa.caltech.edu

I. INTRODUCTION

A worldwide effort is currently underway to build a network of second generation gravitational wave detectors [1–3]. These advanced detectors are designed to achieve approximately ten times higher sensitivities compared to the first generation instruments [4–6]. LIGO operates two observatories in the USA located in Hanford, Washington, and Livingston, Louisiana. The Advanced LIGO detectors are 4 km long enhanced Michelson interferometers [7]. Advanced LIGO started observing in September 2015 and has announced the first discovery of a binary black hole merger [8].

All second generation interferometers adopt the prevailing optical configuration named *dual recycled Fabry-Perot Michelson interferometer*. This configuration is based on the Michelson interferometer with each arm 'folded-up' by Fabry-Perot resonators [9] and with dual recycling which consists of power recycling [10, 11] and signal recycling [12, 13]. Fig. 1 shows a simplified optical layout of such an interferometer. The main mirrors are suspended as pendulums by low-mechanical-loss fibers to provide seismic isolation. Above the lowest pendulum frequency the suspended masses are considered free and able to react to incoming gravitational waves. A high finesse Fabry-Perot resonator in each arm of the Michelson interferometer amplifies the sensitivity by effectively bouncing the field multiple times. This increases the interaction time of the light with gravitational waves. The Michelson interferometer is maintained near a dark fringe, so that only a minimum amount of light leaks out at the antisymmetric port. As a result, a large fraction of the light reflects back towards the laser source. The input side of the Michelson interferometer is equipped with a partially reflecting optic referred to as the power recycling mirror. This additional optical resonator matches the input field to the losses of the interferometer. This increases the laser power on the beam splitter and thus increases the power stored in each arm cavity. Another partially reflecting optic, referred to as the signal recycling mirror, is placed at the output side of the Michelson interferometer. This output optical resonator is used to tune the bandwidth of the detector for observations. The combination of power and signal recycling techniques is collectively referred to as dual recycling.

In order to operate a dual recycled interferometer with high sensitivity, the Michelson degree of freedom and all optical resonators must be held in the vicinity of the desired operating points [14]. The biggest disturbance comes from ground motion which continuously

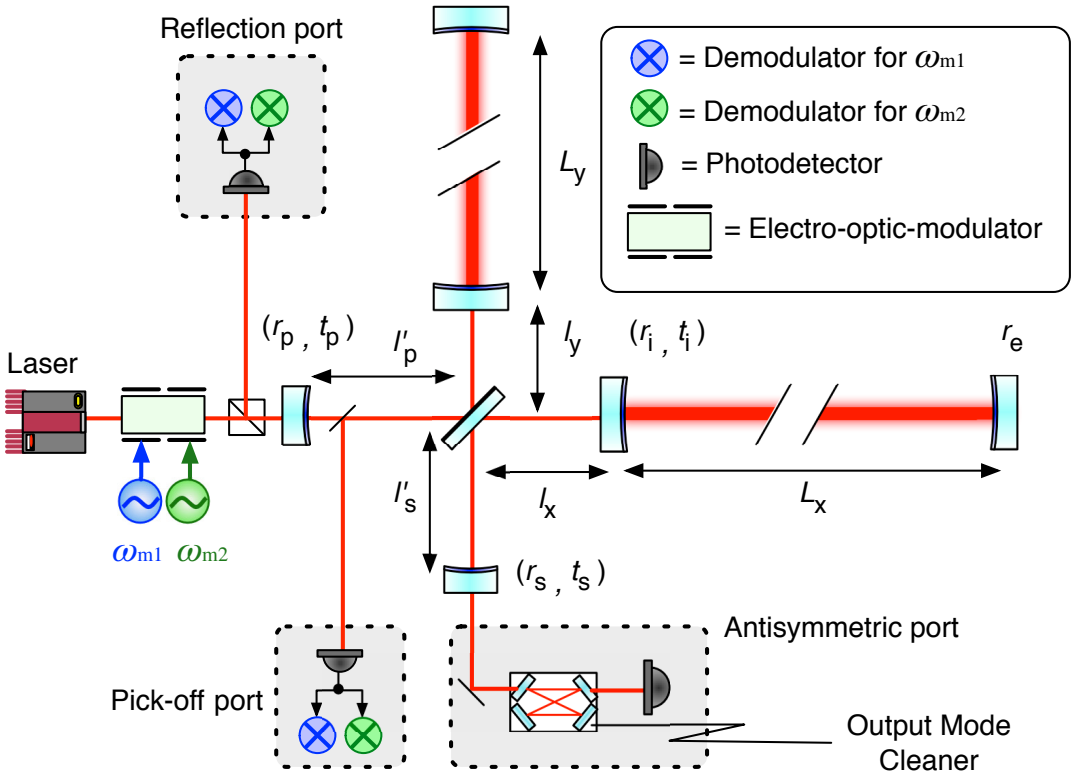

FIG. 1. A simplified optical layout of the dual recycled Fabry-Perot Michelson interferometer. The shown interferometer configuration is common to all second generation gravitational wave antennae, whereas the photodetectors, the electro-optic-modulators and the demodulators are specific to Advanced LIGO.

excites the position of the mirrors by up to several micrometer rms. Below $\simeq$1 Hz the isolation systems can not passively attenuate the vibrations. Active isolation will reduce this motion relative to an inertial reference frame, but practically with a limited performance. Therefore, the microscopic lengths of the cavities and the Michelson interferometer must be controlled by means of feedback control during operations. This in turn requires interferometric sensing of all longitudinal degrees of freedom in the detector. There can be large cross couplings between different degrees of freedom because an optical field in the interferometer can be affected not only by one length degree of freedom but also by other ones due to the field propagating between the multiple coupled optical resonators. It is challenging to robustly decompose the interferometric signals into the individual length degrees of freedom. The cross couplings pose the threat of contaminating the gravitational wave readout by injecting sensing noises from other degrees of freedom. Therefore, it is important to have

a firm understanding of the propagating optical fields and the resulting interference terms which are used for length sensing.

In this paper, we derive analytical expressions for the length sensing and control scheme in Advanced LIGO. This is an extension of the work done for initial detectors [15] and includes the treatment of photon radiation pressure. First, we review the currently implemented scheme in Advanced LIGO which follows the design outlined in [7]. Our analysis is entirely done analytically, in contrast to the original design process [16] which relied on numerical simulations only. Secondly, we generalize the model, so it can be used to improve the design of future terrestrial gravitational wave antennae [17, 18].

We adopt the audio-sideband perturbation technique [19] for deriving the interferometric responses as functions of frequency. The radiation pressure effect is included where it is important. Our analysis confirms that the length sensing can have cross coupled terms not only due to the multiple coupled optical resonators, but also through photon radiation pressure. These cross couplings need to be addressed with a tailored feedback compensation network, as has been done in the actual experiments [20].

The organization of this paper is as follows: In section II we describe the interferometer setup of Advanced LIGO and introduce the optical parameters. In section III we derive the sensing functions for all longitudinal degrees of freedom at various detection ports. Section IV describes the length control scheme and discusses signal diagonalization and noise couplings, both of which depend on the control topology. Finally, we conclude our study in section V.

II. OPTICAL SETUP

A dual recycled Fabry-Perot Michelson interferometer has 5 longitudinal degrees of freedom. Fig. 1 shows a schematic view of the Advanced LIGO optical setup.

We denote the length of the two arm cavities with L_x and L_y, respectively. The lengths between the beamsplitter and the arm cavities are described by l_x and l_y, respectively, whereas the length from the power recycling mirror to the beamsplitter is l'_p and the length from the beamsplitter to the signal recycling mirror is l'_s. Since we are operating the beamsplitter near a dark fringe, it is analytically simpler to treat common and differential modes

separately. We define

$$L_- = \frac{L_x - L_y}{2}, \quad L_+ = \frac{L_x + L_y}{2}, \quad l_- = \frac{l_x - l_y}{2}, \quad l_\mathrm{p} = l'_\mathrm{p} + \frac{l_x + l_y}{2} \quad \text{and} \quad l_\mathrm{s} = l'_\mathrm{s} + \frac{l_x + l_y}{2}. \tag{1}$$

The sixth combination, $l'_\mathrm{p} + l'_\mathrm{s} - (l_x + l_y)$, characterizes the beam splitter common position and is not an independent optical degree of freedom. The 5 optical degrees of freedom are named, in turn: the differential arm cavity length, the common arm cavity length, the Michelson length, the power recycling cavity length and the signal recycling cavity length. In addition, we will include the laser wavelength as another independent longitudinal degree of freedom.

The laser field is generated by a Nd:YAG laser with a wavelength of 1064 nm. Using external amplifier stages, it is capable of delivering a light power of 125 W into the interferometer. The input laser field is phase-modulated at radio-frequencies (RF) by an electro-optic-modulator. For the interferometer sensing two different frequencies are relevant: one at $\omega_\mathrm{m1}/(2\pi) = 9.1$ MHz and the other at exactly 5 times the frequency, $\omega_\mathrm{m2}/(2\pi) = 45.5$ MHz. The RF sidebands frequencies are integer multiples, so that they transmit through an extra optical cavity, referred to as the input mode cleaner (not shown in the figure), between the modulator and the main interferometer.

Using the Jacobi-Anger expansion, we express the phase modulated field as a linear combination of the first five frequency components. We call the fundamental mode the carrier field and refer to the four others as the RF sideband fields. We can then write the input field as

$$E_\mathrm{in} = J_0(\Gamma_1) J_0(\Gamma_2) E_0 e^{i\omega_0 t} \left\{ 1 + i \sum_{v=\pm 1} \left[\frac{J_1(\Gamma_1)}{J_0(\Gamma_1)} e^{vi\omega_\mathrm{m1} t} + \frac{J_1(\Gamma_2)}{J_0(\Gamma_2)} e^{vi\omega_\mathrm{m2} t} \right] \right\}. \tag{2}$$

where E_0 is the input field amplitude, ω_0 is the laser frequency, Γ_1 and Γ_2 are the modulation depths for frequencies ω_m1 and ω_m2, respectively, J_0 and J_1 are the Bessel functions of the first kind and are functions of the modulation depths. We have omitted the second and higher order sidebands because the modulation depths used in the gravitational wave interferometers are typically small and therefore they are insignificant for deriving the interferometric responses in this paper.

The macroscopic length of the power recycling cavity is approximately $l_\mathrm{p} \simeq 58$ m and chosen to be resonant for all frequency components simultaneously. The macroscopic length

of the signal recycling cavity is set to $l_{\rm s} \simeq 56$ m, such that the carrier and the $\omega_{\rm m2}$ sidebands are simultaneously resonant, while the $\omega_{\rm m1}$ are not.

In the normal operating mode of Advanced LIGO, the interference condition for the signal recycling cavity is adjusted such that resonant sideband extraction is achieved [13]. This decreases the effective finesse of the arm cavities for the differential mode and, hence, widens the observational bandwidth, while still maintaining high circulating light power in the arm cavities.

In Advanced LIGO, the Fabry-Perot arm cavities are 4 km long. The length of the Fabry-Perot arm cavities and modulation frequencies are conditioned, so that the carrier is resonant, whereas the RF sidebands are very near the exact point in between. This means that the carrier and RF sidebands experience different arm reflectivity coefficients. We write the reflectivity for the carrier and the sideband fields as

$$r_{\rm a} \equiv \frac{r_{\rm e}\left(t_{\rm i}^2 + r_{\rm i}^2\right) - r_{\rm i}}{1 - r_{\rm i} r_{\rm e}} \quad \text{and} \quad \hat{r_{\rm a}} \equiv -\frac{r_{\rm e}\left(t_{\rm i}^2 + r_{\rm i}^2\right) + r_{\rm i}}{1 + r_{\rm i} r_{\rm e}}, \tag{3}$$

respectively, where $r_{\rm i}$ and $t_{\rm i}$ are the reflectivity and transmissivity of the input mirror, respectively, and $r_{\rm e}$ is the reflectivity of the end mirror. The use of a Fabry-Perot cavity makes the carrier field more sensitive to a small change in the cavity length. This enhancement can be quantified by the derivative of the reflectivity with respect to the round-trip cavity phase. We find for carrier and RF sidebands

$$r_{\rm a}' = \frac{t_{\rm i}^2 r_{\rm e}}{\left(1 - r_{\rm i} r_{\rm e}\right)^2} \quad \text{and} \quad \hat{r_{\rm a}}' = \frac{t_{\rm i}^2 r_{\rm e}}{\left(1 + r_{\rm i} r_{\rm e}\right)^2}, \tag{4}$$

respectively.

The optical properties of the Michelson interferometer can be calculated by replacing the reflectivity coefficients of the input mirrors with the ones above for the Fabry-Perot arm cavities. Since the Michelson interferometer is held at a dark fringe, the Michelson reflectivity for the carrier field is directly given by the average arm cavity reflectivity, $r_{\rm a}$. The Michelson transmissivity to the antisymmetric port for the carrier field is assumed to be zero. On the other hand, the RF sidebands have a finite transmissivity, because of a small macroscopic length offset, referred to as the *Schnupp asymmetry*. It was originally proposed to sense the Michelson degree of freedom [21], but it also plays an important role for sensing the signal recycling cavity length, l_s, in the dual recycled interferometer. Due to the Schnupp asymmetry the Michelson reflectivity and transmissivity for the RF sidebands

become frequency dependent. We can compute the Michelson reflectivity and transmissivity for the RF sidebands fields with

$$r_{\rm m}\left(\omega_{\rm m}\right) = \hat{r_{\rm a}} \cos\left(\frac{2\omega_{\rm m} l_{\rm sch}}{c}\right) \quad \text{and} \quad t_{\rm m}\left(\omega_{\rm m}\right) = \hat{r_{\rm a}} \sin\left(\frac{2\omega_{\rm m} l_{\rm sch}}{c}\right), \tag{5}$$

where $\omega_{\rm m}$ is one of the RF modulation frequencies, and $l_{\rm sch}$ is the Schnupp asymmetry. In Advanced LIGO, the Schnupp asymmetry is chosen to be $2l_{\rm sch} = l_{\rm x} - l_{\rm y} \simeq 0.08$ m.

Due to the dark fringe condition and the symmetry in the Michelson interferometer, the common arm cavity length couples to the power recycling cavity, whereas the differential arm cavity length couples to the signal recycling cavity. It is convenient to characterize them separately by introducing the amplitude gains for the power and signal recycling cavities as

$$g_{\rm p} = \frac{t_{\rm p}}{1 - r_{\rm p} r_{\rm a}} \quad \text{and} \quad g_{\rm s} = \frac{t_{\rm s}}{1 + r_{\rm s} r_{\rm a}}, \tag{6}$$

where $r_{\rm p}$ and $t_{\rm p}$ are the reflectivity and transmissivity of the power recycling mirror, respectively, and where $r_{\rm s}$ and $t_{\rm s}$ are the reflectivity and transmissivity of the signal recycling mirror, respectively. The power recycling gain, $g_{\rm p}$, represents the field amplification factor in the power recycling cavity with respect to the field entering the cavity. The signal recycling gain, $g_{\rm s}$, represents the field amplification factor for a signal generated by a displacement in the differential arm length. In the case of resonant sideband extraction, the signal recycling gain is smaller than unity by definition, because it widens the observation bandwidth at a cost of the readout gain. In Advanced LIGO, the power recycling gain has been experimentally determined to be $g_{\rm p}^2 \simeq 40$, whereas the signal recycling gain is expected to be $g_{\rm s}^2 \simeq 0.1$.

We introduce two characteristic frequencies, both of which are called cavity poles. The first one accounts for the frequency response of the common carrier field to the combined power recycling and arm cavity system, whereas the second one accounts for the response of the differential carrier field to the combined signal recycling and arm cavity system. We define them as

$$\omega_{\rm cc} = \frac{c}{2L_+} \ln\left(\frac{1 + r_{\rm i} r_{\rm p}}{r_{\rm e} r_{\rm i} + r_{\rm e} r_{\rm p}\left(r_{\rm i}^2 + t_{\rm i}^2\right)}\right) \quad \text{and} \quad \omega_{\rm rse} = \frac{c}{2L_+} \ln\left(\frac{1 - r_{\rm i} r_{\rm s}}{r_{\rm e} r_{\rm i} - r_{\rm e} r_{\rm s}\left(t_{\rm i}^2 + r_{\rm i}^2\right)}\right). \tag{7}$$

In Advanced LIGO, the common cavity pole is approximately $\omega_{\rm cc}/(2\pi) \simeq 0.5$ Hz, whereas the differential cavity pole is set to $\omega_{\rm rse}/(2\pi) \simeq 380$ Hz with $t_{\rm s}^2 = 35\%$. In the subsequent sections, we often refer to these cavity poles in the Laplace notation with $s_{\rm cc} = i\omega/\omega_{\rm cc}$ and $s_{\rm rse} = i\omega/\omega_{\rm rse}$.

Describing the RF sidebands in the dual recycled Michelson interferometer is not as straightforward as that for the carrier due to the presence of the Schnupp asymmetry. The asymmetry breaks the clean separation between the power and signal recycling cavities. Generally, the RF sidebands can propagate between the two recycling cavities. One way to compute this effect is to include the signal recycling mirror in the Michelson reflectivity and transmissivity calculation. In Advanced LIGO, the signal recycling cavity length is conditioned, so that the higher frequency RF sideband pair is resonant, whereas the lower frequency one is not. We can then write the reflectivity and transmissivity of the signal recycled Michelson as

$$r_{\rm sm} = \frac{r_{\rm m} \mp \hat{r_{\rm a}}^2 r_{\rm s}}{1 \mp r_{\rm s} r_{\rm m}} \quad \text{and} \quad t_{\rm sm} = \frac{t_{\rm s} t_{\rm m}}{1 \mp r_{\rm s} r_{\rm m}}, \tag{8}$$

where the upper signs represent the lower frequency RF sideband pair, $\omega_{\rm m1}$, and where the lower signs represent the higher frequency RF sideband pair, $\omega_{\rm m2}$. We will keep using this sign convention throughout the paper.

Using the reflectivity of the signal recycled Michelson, $r_{\rm sm}$, one can compute the power recycling gain for the RF sidebands as

$$g_{\rm sb} = \frac{t_{\rm p}}{1 + r_{\rm p} r_{\rm sm}}. \tag{9}$$

In Advanced LIGO, the RF sideband gains in the power recycling cavity are $g^2_{{\rm sb},\omega_{\rm m1}} \simeq 127$ and $g^2_{{\rm sb},\omega_{\rm m2}} \simeq 18$ for the lower and higher frequency sidebands, respectively. We can also define the carrier and RF sideband reflectivity for the entire interferometer with

$$r_{\rm c} = \frac{\left(r_{\rm p}^2 + t_{\rm p}^2\right) r_{\rm a} - r_{\rm p}}{1 - r_{\rm p} r_{\rm a}} \quad \text{and} \quad r_{\rm sb} = -\frac{\left(r_{\rm p}^2 + t_{\rm p}^2\right) r_{\rm sm} + r_{\rm p}}{1 + r_{\rm p} r_{\rm sm}}. \tag{10}$$

Advanced LIGO senses all length degrees of freedom at 3 different ports using photodetectors, see Fig. 1. The common arm cavity length is sensed in reflection of the interferometer, whereas the power and signal recycling cavity lengths as well as the Michelson length are sensed at the pick-off port. The pick-off port samples the beam returned by the beamsplitter inside the power recycling cavity. The differential arm cavity length is sensed at the antisymmetric port. All signals, except the ones sensed at the antisymmetric port, are encoded on beat notes at the RF sideband frequencies and need to be demodulated first.

For detecting gravitational waves Advanced LIGO employs a DC readout scheme [22]. During operations the arm cavities are pushed slightly off resonance, in order to produce a

static carrier field at the antisymmetric port. Now, a small differential length change will linearly change the amount of carrier light at the antisymmetric port. Both RF demodulation and DC readout can sense the differential length change at the antisymmetric port, but the DC readout scheme is more sensitive.

In the DC readout path, the light field is optically filtered by a bow-tie shaped resonator called the output mode cleaner. It attenuates undesired field components, such as spatial higher order modes and RF sidebands, which would contribute extra shot noise to the photodetector sensing. For simplicity in our analysis, we assume the output mode cleaner to be lossless and thus the transmissivity for the carrier to be unity. On the other hand, the RF sidebands are significantly attenuated. For instance, the power transmitted at the ω_{m2} sideband frequency is expected to be 60 ppm only. However, we should note that such small transmission can add significant amount of noise through laser intensity noise coupling [22, 23].

III. LENGTH READOUT SCHEME

A. Overview

The length sensing scheme for Advanced LIGO is similar to initial LIGO [15, 22] for all degrees of freedom with the exception of the signal recycling cavity. Adding signal recycling necessitates the use of two sets of RF modulation frequencies to robustly separate power and signal recycling cavity lengths. Three different interferometric readout techniques are used in Advanced LIGO. The homodyne or DC readout technique [22] senses the differential arm cavity length, L_-. The Pound-Drever-Hall technique [24] senses the common arm length, L_+, as well as the two recycling cavity lengths, l_{p} and l_{s}. Finally, the Schnupp technique [21] senses the Michelson length, l_-.

For DC readout, the differential arm length is intentionally displaced by a few to 10 picometers. We express the DC offset in terms of the optical phase shift as

$$\epsilon = kL_{\mathrm{offset}}, \tag{11}$$

with k the wave number, and L_{offset} the actual displacement introduced by the differential arm length offset. When L_- is dynamically disturbed by a small amount through external forces, such as gravitational waves or seismic motion, it produces a pair of audio sidebands

around the carrier field due to the small deviation in the optical length. The audio sidebands propagate to the antisymmetric port and interfere with the carrier static field which serves as the local oscillator. The resulting intensity modulation measured by the photodetector is then proportional to the differential arm displacement. Ideally, the RF sidebands are stripped away by the output mode cleaner, and have no effect on the DC readout scheme.

The RF readouts, including the Pound-Drever-Hall and the Schnupp techniques, generally measure carrier signals by comparing them to the RF sidebands which serve as the local oscillator fields. However, in the case of the Michelson length, it is the other way around: the signal is carried by the RF sidebands, and the carrier serves as the local oscillator field. Moreover, the power and signal recycling cavity lengths are more involved; there are also terms that are generated by the RF sidebands with the static carrier field serving as the local oscillator.

When a length degree of freedom is disturbed by a small amount, it produces a phase-shift on the light field, or equivalently a pair of audio sidebands. The audio sidebands are generated around both the carrier and the RF sideband fields, but in general have different amplitudes. For a cavity where the carrier field is resonant and the RF sidebands are not, the audio sidebands on the carrier field will dominate and generate a signal by beating against the static RF sideband fields. In this case, the RF sidebands serve as the local oscillator field. Since a photodetector is a square-law detector, pure phase modulation signals are not sensed. The key advantage of the Pound-Drever-Hall technique is that a cavity will only return amplitude modulated light when off resonance. Hence, this technique allows the implementation of highly sensitive null servos.

Our derivation includes radiation pressure effects, where they matter. They arise due to the intentional offset in the arm cavities in conjunction with the high circulating cavity power. Assuming arm cavity losses of the order of 80 ppm and all the laser power is consumed by the arm cavity losses, one can estimate the maximum circulating power to be $P_{\rm in}/(2 \times 80 \text{ ppm}) \simeq 780$ kW. The factor of two comes from the beam splitter ratio, and $P_{\rm in}$ is the input laser power defined as $P_{\rm in} = |E_{\rm in}|^2$ and taken to be 125 W. Advanced LIGO uses 40 kg test masses suspended by $\simeq 1$ m long fibers. A megawatt of light will exert a significant force through radiation pressure and will alter the dynamics of the test mass. If a cavity is near resonance, a change in length will introduce a change in the circulating power. In return, this change in power, will feed back to the length through the dynamics

of the suspended test mass. If the change in power is represented by ΔP, we can calculate the induced length change by using

$$\Delta L = \frac{2\Delta P}{c s_\mu^2}, \quad \text{with} \quad s_\mu^2 = -\mu\omega^2 \quad \text{and} \quad \mu = \frac{m_\mathrm{i} m_\mathrm{e}}{m_\mathrm{i} + m_\mathrm{e}}, \tag{12}$$

where s_μ is the mechanical response of the test mass in the Laplace notation, m_i and m_e are the masses of the input and end mirrors, respectively, and μ is the reduced mass of the system.

In our derivation we do not include optical spring effects [25] which modify the mechanical response of the suspended test masses through the feedback mechanism described above. Instead, we approximate the mirrors as free test masses. This will introduce large discrepancies between our equations and the exact solutions at low frequencies. Typically, below 10 Hz the dynamics of the test masses is governed by optical spring effects in the presence of high circulating power. In this paper, we are mainly interested in higher frequencies which are relevant for the stability of the servo systems and which matter for gravitational wave detection. Another category of radiation pressure induced dynamical effects are parametric instabilities [26]. We can also neglect them here, since their resonance modes are at frequencies well above the gravitational wave band of interest.

B. DC readout at the antisymmetric port

The DC readout at the antisymmetric port is primarily sensitive to the differential degrees of freedom. The differential modes are read using the static carrier field as a local oscillator field. The response scales linearly with the amplitude of the local oscillator field, which is proportional to the differential arm cavity offset, ϵ. The addition of this offset also introduces a linear coupling for the radiation pressure. As a result, two extra terms proportional to the power and signal recycling cavity lengths are added.

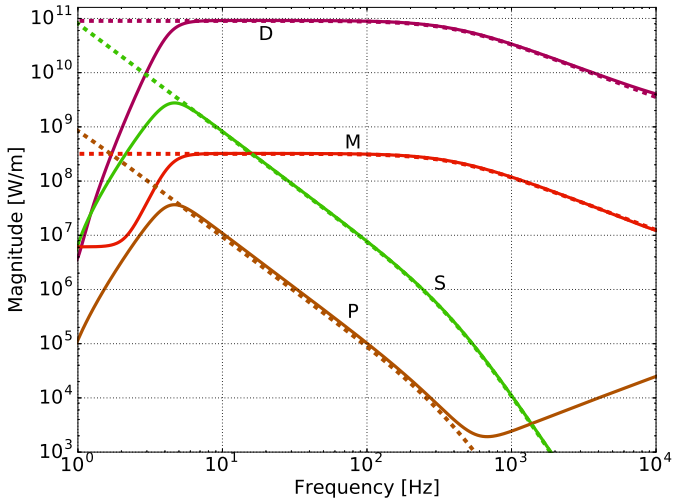

FIG. 2. Magnitude response at the antisymmetric port as functions of frequency. The dashed lines are analytically derived as shown in Eq. (13). They are compared against numerically computed solutions [27] depicted with solid lines. The annotation letters denote the following degrees of freedom: (D) differential arm cavity length, (M) Michelson length, (P) power recycling cavity length and (S) signal recycling cavity length. The discrepancies below 10 Hz are due to optical springs which are not included in the derivation. The discrepancy in the response of the power recycling cavity length above 700 Hz is due to omission of the Schnupp asymmetry. The numerical parameters are given in Table I of the Appendix.

The response, normalized by the $S_{\rm dc} = 2J_0^2(\Gamma_1)J_0^2(\Gamma_2)P_{\rm in}$, can be written as

$$\begin{aligned}\frac{S_{\rm as}}{S_{\rm dc}} =& 4g_{\rm p}^2 g_{\rm s}^2 r_{\rm a}'^2 \epsilon \frac{k\Delta L_-}{1+s_{\rm rse}} \\ &+ 4g_{\rm p}^2 g_{\rm s}^2 r_{\rm a}' r_{\rm a} \epsilon \frac{k\Delta l_-}{1+s_{\rm rse}} \\ &+ 4g_{\rm p}^2 g_{\rm s}^2 r_{\rm a}'^2 \epsilon \left(\frac{\partial L_-}{\partial l_p}\right) \frac{k\Delta l_{\rm p}}{1+s_{\rm rse}} \\ &+ 4g_{\rm p}^2 g_{\rm s}^2 r_{\rm a}'^2 \epsilon \left(\frac{\partial L_-}{\partial l_s}\right) \frac{k\Delta l_{\rm s}}{1+s_{\rm rse}},\end{aligned} \tag{13}$$

where $\partial L_-/\partial l_{\rm p}$ and $\partial L_-/\partial l_{\rm s}$ are dimensionless opto-mechanical couplings due to the radiation pressure. They are defined as

$$\frac{\partial L_-}{\partial l_p} = \frac{4g_{\rm p}g_{\rm s}^2 r_{\rm a}'\left(1+r_{\rm a}r_{\rm p}\right)s_{\rm rse}}{ct_{\rm p}s_\mu^2\left(1+s_{\rm cc}\right)\left(1+s_{\rm rse}\right)}\epsilon k P_{\rm a} \quad \text{and} \quad \frac{\partial L_-}{\partial l_s} = \frac{16g_{\rm s}^2 r_{\rm a}' r_{\rm s}}{ct_{\rm s}^2 s_\mu^2\left(1+s_{\rm rse}\right)}\epsilon k P_{\rm a}, \tag{14}$$

where $P_{\rm a} = P_{\rm in}\left[J_0(\Gamma_1)J_0(\Gamma_2)g_{\rm p}r_{\rm a}'\right]^2/2$ is the circulating laser power in an arm cavity.

The magnitude response of each term is shown as a function of frequency in Fig. 2. The analytical expressions show excellent agreement with numerical plane wave simulations in the frequency domain [27] over most of the frequency band of interest. As expected, the analytical calculations differ from the numerical simulations below 10 Hz due to the omission of the optical spring. In addition, the power recycling cavity length differs at frequencies above 700 Hz, because we have omitted the effect of the Schnupp asymmetry for this effect. Since the displacement of the power recycling cavity length at such high frequencies is strongly attenuated by the seismic isolation system and the suspensions, this has no practical consequences.

Not surprisingly, the most significant term in Eq. (13) is due to the differential arm cavity length. The size of the response is amplified by the square of the two recycling gains $g_{\rm p}^2 g_{\rm s}^2$, even though, the absolute size of the signal depends on the offset ϵ. Changing the offset, in principle, does not change the shot-noise-limited sensitivity, because the shot-noise level scales with ϵ as well. The response function sees the cavity pole due to the resonant sideband extraction at $\omega_{\rm rse}/(2\pi) \simeq 380$ Hz.

The second term in Eq. (13) represents the Michelson length. The functional form is the same as for the differential arm, except that the size of the signal is smaller by the ratio $r'_{\rm a}/r_{\rm a}$. This ratio is approximately 280 in Advanced LIGO. The ratio comes from the amplification by the Fabry-Perot arm cavities, which is imposed on the differential arm cavity length, but not on the Michelson length. Since there is no way to separate differential arm from Michelson motion at the antisymmetric port, the Michelson length has to be sensed by another photodetection port. This in turn can introduce additional noise at the antisymmetric port, if the residual Michelson motion cannot be suppressed far enough.

The third term in Eq. (13) is due to the power recycling cavity length, which couples to the DC readout signal through the radiation pressure effect. A change of the power recycling cavity length introduces a small frequency shift of the carrier light incident to the beamsplitter, and hence incident to the Fabry-Perot arm cavities. This frequency shift in turn will affect the circulating arm cavity powers with opposite sign, since the two arm cavities have been pushed off resonance in opposite directions by the DC offset. This is the same mechanism responsible for the coupling of laser frequency noise to the antisymmetric port [28]. The overall transfer function in Eq. (13) falls as f^{-2} due to the dynamical response of the suspended test masses in frequency band from $\omega_{\rm cc}/(2\pi) \simeq 0.5$ Hz to $\omega_{\rm rse}/(2\pi) \simeq$

380 Hz. A unique feature of the radiation pressure couplings in Eq. (14) is that they scale with both the circulating arm cavity power, $P_{\rm a}$, and the DC offset, ϵ.

The last term in Eq. (13) is due to the signal recycling cavity length. It was first discovered through numerical simulations [16]. The coupling mechanism differs from the one of the power recycling cavity length. A perturbation of the signal recycling cavity length creates a pair of phase-modulated audio sidebands around the carrier light which is the local oscillator field for the DC readout. To first order they do not produce a signal at the antisymmetric port. However, when the audio sidebands enter the arm cavities, they will modulate the amplitude of the circulating field. This effect can be large, because the audio sidebands directly couple to the large circulating fields in the arm cavities. As with the coupling from the power recycling cavity, the resulting response experiences the suspension dynamics and falls as f^{-2} at low frequencies. Again, the size of the opto-mechanical coupling scales with the circulating arm cavity power and the DC offset. Around 10 Hz, the effect can be as large as for the Michelson length, but falls rapidly as f^{-2} at frequencies above.

C. RF readout at the reflection port

The signal measured at the reflection port using RF demodulation at $\omega_{\rm m}$ contains terms from all five length degrees of freedom as well as a term from the laser frequency. The signal at the reflection port is primarily sensitive to the common mode degrees of freedom of the interferometer. To condense the result, we introduce the normalization factor $S_{\rm rf}(\omega_{\rm m}) = 2J_0(\Gamma_{\rm m})J_1(\Gamma_{\rm m})J_0^2(\Gamma_{\rm n})P_{\rm in}$, with $\Gamma_{\rm m}$ and $\Gamma_{\rm n}$ the modulation depths at the RF demodulation frequencies, $\omega_{\rm m}$ and $\omega_{\rm n}$, respectively. The modulation frequency, $\omega_{\rm n}$, is the one not used in the demodulation.

The response for the RF demodulation at frequency $\omega_{\rm m}$ can be summarized as

$$\begin{aligned}\frac{S_{\rm refl}}{S_{\rm rf}} =& -4g_{\rm p}^2 r'_{\rm a} r_{\rm sb} \frac{k\Delta L_+}{1+s_{\rm cc}} \cos\omega_{\rm m} t \\ &+ 4g_{\rm sb}^2 r_{\rm c} \hat{r_{\rm a}}' \chi k\Delta L_- \sin\omega_{\rm m} t \\ &- 4g_{\rm sb}^2 r_{\rm c} \hat{r_{\rm a}} \chi k\Delta l_- \sin\omega_{\rm m} t \\ &- 4\left(g_{\rm p}^2 r_{\rm a} r_{\rm sb} + g_{\rm sb}^2 r_{\rm c} r_{\rm sm}\right) \frac{1+s_{\rm pr}}{1+s_{\rm cc}} k\Delta l_{\rm p} \cos\omega_{\rm m} t \\ &\mp 4\frac{\left(t_{\rm c}^2 r_{\rm sb} - g_{\rm sb}^2 r_{\rm c} t_{\rm sm}^2\right) r_{\rm s}}{t_{\rm s}^2} \frac{1+s_{\rm sr}}{1+s_{\rm cc}} k\Delta l_{\rm s} \cos\omega_{\rm m} t \\ &- 4g_{\rm p}^2 r'_{\rm a} r_{\rm sb} \frac{kL_+}{1+s_{\rm cc}} \left(\frac{\Delta\nu}{\nu_0}\right) \cos\omega_{\rm m} t,\end{aligned} \tag{15}$$

where ν_0 and $\Delta\nu$ are the laser frequency and a small change in the laser frequency, respectively, and where we have introduced the frequency independent coefficient, χ, which is defined as

$$\chi = \frac{1 - r_{\rm s}^2 \hat{r_{\rm a}}^2}{\left(1 \mp r_{\rm s} r_{\rm m}\right)^2} \sin\left(\frac{2\omega_{\rm m} l_{\rm sch}}{c}\right). \tag{16}$$

This coefficient represents the coupling of the differential modes to the reflection port for the RF sidebands. We have also introduced the interferometer transmission of the carrier field to the antisymmetric port as

$$t_c = 2g_{\rm p} g_{\rm s} r'_{\rm a} \epsilon. \tag{17}$$

The frequencies, $\omega_{\rm pr} = i\omega/s_{\rm pr}$ and $\omega_{\rm sr} = i\omega/s_{\rm sr}$, describe the zeros in the responses of the power and signal recycling cavities, respectively. They are defined with

$$\frac{\omega_{\rm pr}}{\omega_{\rm cc}} = 1 + \frac{g_{\rm p}^2 r_{\rm a} r_{\rm sb}}{g_{\rm sb}^2 r_{\rm c} r_{\rm sm}} \quad \text{and} \quad \frac{\omega_{\rm sr}}{\omega_{\rm cc}} = 1 - \frac{t_{\rm c}^2 r_{\rm sb}}{g_{\rm sb}^2 r_{\rm c} t_{\rm sm}^2}. \tag{18}$$

Since the terms in Eq. (15) are due to RF modulation, they can be aligned in-phase with the modulation, $\cos\omega_{\rm m} t$, or aligned with the quadrature phase, $\sin\omega_{\rm m} t$. Quadrature phase signals are produced with the carrier serving as the local oscillator. Due to the Schnupp asymmetry a differential length change will result in upper and lower RF sidebands to be reflected by the beamsplitter with unequal amplitude. This causes the RF sidebands to be the primary conveyer of differential displacement information in reflection. The efficiency of the RF sidebands to be able to transmit to the reflection port is characterized by χ. As seen in Eq. (16), it is a function of the both the modulation frequency and the Schnupp asymmetry. Since the RF sidebands are not resonant in the Fabry-Perot arm cavities, their response as function of frequency is flat in the band of interest.

The dominant length term in Eq. (15) is due to the common arm cavity length. This signal is produced by the RF sidebands serving as local oscillator fields, whereas the carrier experiences a phase shift in the Fabry-Perot arm cavities. Since the carrier field is resonant in both the arm cavities and the power recycling cavity, it sees the common cavity pole, $s_{\rm cc}$. The size of the signal depends on the amplitude of the available local oscillator field which is quantified by sideband reflectivity, $r_{\rm sb}$.

The second and third terms in Eq. (15) are due to the differential arm length and the Michelson length, respectively. Both are quadrature phase signals and scale with the amount of the reflected RF sideband fields, $r_{\rm c}$. The magnitude of the response of the Michelson length is larger than that of the differential arm cavity length by the ratio $\hat{r}_{\rm a}/\hat{r}'_{\rm a}$. This is a consequence of the fact that the arm cavities are off resonance for the RF sidebands and, therefore, highly inefficient in exciting them.

The fourth and fifth terms in Eq. (15) are due to the power and signal recycling cavity lengths, respectively. Because both degrees of freedom can efficiently excite the audio sidebands of not only the carrier but also the RF sideband fields simultaneously, their responses are more involved. Both responses contain a pole-zero pair, which is a consequence of the signals being composed of two terms each. One of the terms is using the RF sidebands as the local oscillator and sees the common cavity pole, whereas the other term uses the carrier as the local oscillator and sees no frequency dependency. In total, their responses are more complicated and contain a pole-zero pair. The signals are in-phase. One big difference in the signal recycling cavity response is that the amplitude of the carrier term is a function of the differential arm offset, ϵ. This is a consequence of the available DC carrier light in the signal recycling cavity being determined by $t_{\rm c}/t_{\rm s} \propto \epsilon$. In turn, differential arm offset affects the location of the zero, $\omega_{\rm sr}$, as well as the gain at low frequencies.

The last term in Eq. (15) is due to the laser frequency. It has the same functional form as the term from the common arm cavity length. In fact, they are equivalent, if we make use of the well-known relation $\Delta\nu/\nu_0 = \Delta L_+/L_+$.

D. RF readout at the pick-off port

The signals at the pick-off port are very similar to the ones at the reflection port. The differences arise mainly due to the different amount of the local oscillator fields available.

The response at the pick-off port can be written as

$$\begin{aligned}\frac{S_{\rm pop}}{S_{\rm rf}} =& \frac{4g_{\rm p}^2 g_{\rm sb} r_{\rm a}' r_{\rm sm}}{t_{\rm p}} \frac{1}{1+s_{\rm cc}} k\Delta L_+ \cos\omega_{\rm m} t \\ &+ 4\frac{g_{\rm p} g_{\rm sb}^2 r_{\rm a} \hat{r_{\rm a}}'}{t_{\rm p}} \chi k\Delta L_- \sin\omega_{\rm m} t \\ &- 4\frac{g_{\rm p} g_{\rm sb}^2 r_{\rm a} \hat{r_{\rm a}}}{t_{\rm p}} \chi k\Delta l_- \sin\omega_{\rm m} t \\ &+ 4\left(g_{\rm p} - g_{\rm sb}\right) \frac{g_{\rm p} g_{\rm sb} r_{\rm a} r_{\rm sm}}{t_{\rm p}} \frac{1+s_{\rm pp}}{1+s_{\rm cc}} k\Delta l_{\rm p} \cos\omega_{\rm m} t \\ &\pm 4\frac{g_{\rm sb} r_{\rm s}\left(r_{\rm sm} t_{\rm c}^2 + g_{\rm p} g_{\rm sb} r_{\rm a} t_{\rm sm}^2\right)}{t_{\rm p} t_{\rm s}^2} \frac{1+s_{\rm sp}}{1+s_{\rm cc}} k\Delta l_{\rm s} \cos\omega_{\rm m} t \\ &+ \frac{4g_{\rm p}^2 g_{\rm sb} r_{\rm sm} r_{\rm a}'}{t_{\rm p}} \frac{kL_+}{1+s_{\rm cc}} \left(\frac{\Delta\nu}{\nu_0}\right) \cos\omega_{\rm m} t,\end{aligned} \tag{19}$$

where the frequencies, $\omega_{\rm pp} = i\omega/s_{\rm pp}$ and $\omega_{\rm sp} = i\omega/s_{\rm sp}$, represent zeros in the responses of the power and signal recycling cavity lengths, respectively. They are defined as

$$\frac{\omega_{\rm pp}}{\omega_{\rm cc}} = 1 - \frac{g_{\rm p}}{g_{\rm sb}} \quad \text{and} \quad \frac{\omega_{\rm sp}}{\omega_{\rm cc}} = 1 + \frac{r_{\rm sm} t_{\rm c}^2}{g_{\rm p} g_{\rm sb} r_{\rm a} t_{\rm sm}^2}. \tag{20}$$

Qualitatively, the pick-off port is rich in the local oscillator field of the carrier. On the one hand, the response functions that utilize the carrier field as a local oscillator will benefit from the large local oscillator field in terms of the signal to noise ratio. On the other hand, the response functions that utilize the RF sideband fields as local oscillators suffer from high carrier power, which limits the detectable laser power on the photodetector.

IV. LENGTH CONTROL COMPENSATION NETWORK

The length control compensation network is a critical building block for designing a low noise gravitational wave interferometer. Dual recycled interferometers can be treated as multiple-input and multiple-output (MIMO) systems. Whenever possible, our design will strive to sense the degrees of freedom in the common and differential basis, and then use diagonal controls for individual lengths. It is not always possible to achieve this directly without compromising the noise performance of the gravitational wave readout. However, it is generally feasible to reduce the noise couplings by either implementing a gain hierarchy or by choosing linear combinations of actuators that have minimum couplings to the gravitational wave readout port.

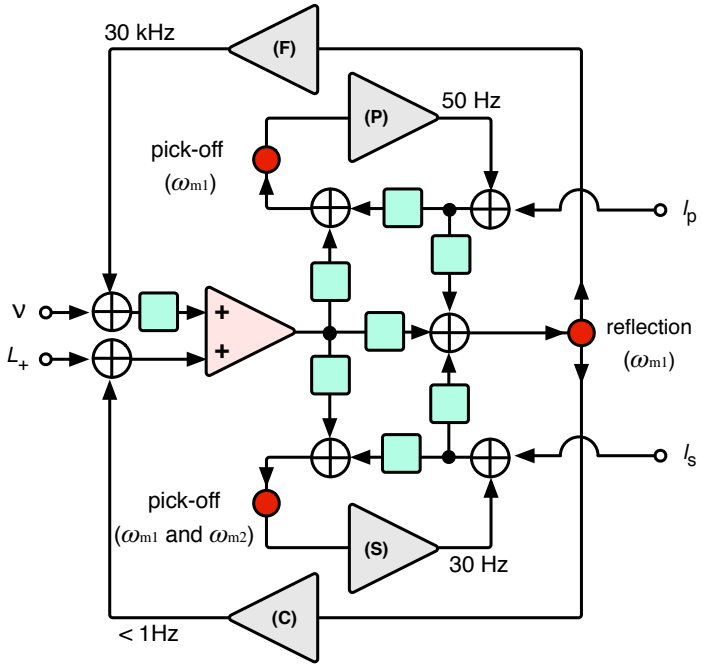

FIG. 3. A block diagram of the common mode control network used by Advanced LIGO. A red disk represents a photodetector. A triangle indicates a user-configurable servo control filter. A rectangular block represents a sensing coefficient which, in general, is a function of frequency. The annotations are as follows: (F) fast feedback for correcting the laser frequency, ν, using the $\omega_{\rm m1}$ demodulated signal in reflection, (C) feedback control for the common arm cavity length, L_+, using the same signal as the laser frequency control, but with a much lower bandwidth of less than 1 Hz, (P) feedback control for the power recycling cavity length, $l_{\rm p}$, using the $\omega_{\rm m1}$ demodulated signal from the pick-off port, and (S) feedback control for the signal recycling cavity length, $l_{\rm s}$, using a linear combination of the $\omega_{\rm m1}$ and $\omega_{\rm m2}$ demodulated signals from the pick-off port.

A. Control of the common modes

The common modes include the common arm cavity length, L_+, the two recycling-cavity lengths, $l_{\rm p}$ and $l_{\rm s}$, and the laser frequency, ν. A simplified block diagram for the common mode control is shown in Fig. 3. The control loop for the common arm-cavity length uses the first set of RF sidebands, $\omega_{\rm m1} \simeq 9.1$ MHz, in reflection. This sensor feeds back to the laser frequency at frequencies above $\simeq 1$ Hz, employing a high bandwidth analog servo with a unity gain frequency of a few 10 kHz. At frequencies below $\simeq 1$ Hz, the dominant motion is due to seismic excitations and due to tidal deformation of the Earth which are

typically several 100 μm peak-to-peak. These low frequency motions are fed back to the mirror positions rather than the laser frequency. The frequency actuator in Advanced LIGO is essentially the same as that of initial LIGO [15] which involves a number of additional optical and electronics elements (not shown in Fig. 1 or 3).

Suppressing frequency noise and common arm cavity length motions with a high gain and high bandwidth servo loop essentially zeros the in-phase signal in reflection for the first set of RF sidebands. This in turn will suppress the corresponding frequency noise signal at the pick-off port—making this signal sensitive to the power recycling cavity motion only. Hence, power recycling cavity length is read out by the pick-off port using the first set of RF sidebands, $\omega_{\rm m1}$, and fed back to the position of the power recycling mirror with a control bandwidth of about 50 Hz. Finally, the signal recycling cavity length can be derived from the pick-off port as well, using a linear combination of the in-phase signals by the two RF sideband sets, $\omega_{\rm m1}$ and $\omega_{\rm m2} \simeq 45.5$ MHz. This combination is chosen so as to be insensitive to the power recycling cavity length and is fed back to the signal recycling mirror with a bandwidth of about 30 Hz. To further analyze the effect of the gain hierarchy, we set the left hand side of Eq. (15) to zero. We also drop the differential degrees of freedom which appear in the quadrature phase. We then obtain the remaining signals at the pick-off port by substituting the result back into Eq. (19).

First, let us take a look at the pick-off port demodulating by $\omega_{\rm m1}$. The response (19) now takes a rather simple form

$$\left.\frac{S_{\rm pop}}{S_{\rm rf}}\right|_{\substack{\omega_{\rm m1}\\ \rm refl=0}} = -4kZ\left[r_{\rm sm}\Delta l_{\rm p} - \left(\frac{t_{\rm sm}}{t_{\rm s}}\right)^2 r_{\rm s}\Delta l_{\rm s}\right]\cos\omega_{\rm m1}t$$
$$\text{with}\quad Z = g_{\rm sb}^2\frac{g_{\rm p}r_{\rm sb}r_{\rm a} + g_{\rm sb}r_{\rm c}r_{\rm sm}}{t_{\rm p}r_{\rm sb}}, \tag{21}$$

where all parameters are associated with the $\omega_{\rm m1}$ RF sidebands and where Z is an amplification gain.

The above equations no longer carry any dependency on the common arm cavity length or the laser frequency. Hence, they can be directly used to sense the recycling cavity lengths. Furthermore, the term from the power recycling cavity length is much larger than that to the one from the signal recycling cavity length by more than five orders of magnitude. This is because of the small coupling of the $\omega_{\rm m1}$ RF sidebands to the signal recycling cavity, i.e., $t_{\rm sm}^2 \ll 1$. As an additional benefit, the frequency dependency has also vanished, resulting in

a simplified servo controller. This was also the case in initial LIGO [15].

Next, we look at the pick-off port demodulating by ω_{m2}. The resulting signal becomes

$$\begin{aligned}\left.\frac{S_{\mathrm{pop}}}{S_{\mathrm{rf}}}\right|_{\substack{\omega_{\mathrm{m2}}\\ \mathrm{refl}=0}} &= -4k\left[r_{\mathrm{sm}}Y_{\mathrm{p}}\Delta l_{\mathrm{p}} + r_{\mathrm{s}}\left(\frac{t_{\mathrm{sm}}}{t_{\mathrm{s}}}\right)^2 Y_{\mathrm{s}}\Delta l_{\mathrm{s}}\right]\cos\omega_{\mathrm{m2}}t,\\ Y_{\mathrm{p}} &= \frac{g_{\mathrm{sb}}^{\mathrm{m2}}}{t_{\mathrm{p}}r_{\mathrm{sb}}^{\mathrm{m1}}}\left[g_{\mathrm{p}}g_{\mathrm{sb}}^{\mathrm{m2}}r_{\mathrm{sb}}^{\mathrm{m1}}r_{\mathrm{a}} + \left(g_{\mathrm{sb}}^{\mathrm{m1}}\right)^2 r_{\mathrm{c}}r_{\mathrm{sm}}^{\mathrm{m1}}\right],\\ Y_{\mathrm{s}} &= \frac{g_{\mathrm{sb}}^{\mathrm{m2}}}{t_{\mathrm{p}}r_{\mathrm{sb}}^{\mathrm{m1}}}\left[g_{\mathrm{p}}g_{\mathrm{sb}}^{\mathrm{m2}}r_{\mathrm{sb}}^{\mathrm{m1}}r_{\mathrm{a}} - \left(g_{\mathrm{sb}}^{\mathrm{m1}}\right)^2 r_{\mathrm{c}}r_{\mathrm{sm}}^{\mathrm{m2}}\left(\frac{t_{\mathrm{sm}}^{\mathrm{m1}}}{t_{\mathrm{sm}}^{\mathrm{m2}}}\right)^2\right],\end{aligned} \tag{22}$$

where we have neglected a term associated with the DC carrier field in the signal recycling cavity by assuming $t_{\mathrm{c}}^2 \ll 1$. The coefficients, Y_{p} and Y_{s}, are again independent of frequency. We are using the superscripts m1 and m2 to indicate, whether the coefficient is associated with the ω_{m1} or the ω_{m2} RF sidebands, respectively.

Evaluating the response to the recycling cavity lengths, one finds that the term from the signal recycling cavity is still smaller than the one from the power recycling cavity by a factor of approximately 10. This gain difference arises from the small finesse of the signal recycling cavity which is about 10 for the ω_{m2} RF sidebands, whereas the finesse of the power recycling cavity for the ω_{m2} RF sidebands is about 70. As a consequence the signal recycling cavity length is derived from a combination of the two in-phase pick-off signals, formed to be insensitive to the power recycling cavity length.

In principle, there is the possibility to sense the signal recycling cavity length in reflection using the ω_{m2} RF sidebands. The situation here is similar to the pick-off port with the added complication that the signal is directly proportional to the reflected carrier field, described by r_{c}. In Advanced LIGO, the power recycling gain for the carrier is chosen to maximize the circulating arm cavity power, and, hence, minimize the reflected carrier power. There is the risk that r_{c} may become zero, or even change the sign depending on losses of the interferometer. Thus, sensing the signal recycling cavity length at the pick-off port is the preferred solution.

B. Control of the differential modes

The differential modes include the differential arm cavity length, L_-, the Michelson length, l_-, and to a certain degree the signal recycling cavity length, l_{s}. Fig. 4 shows a

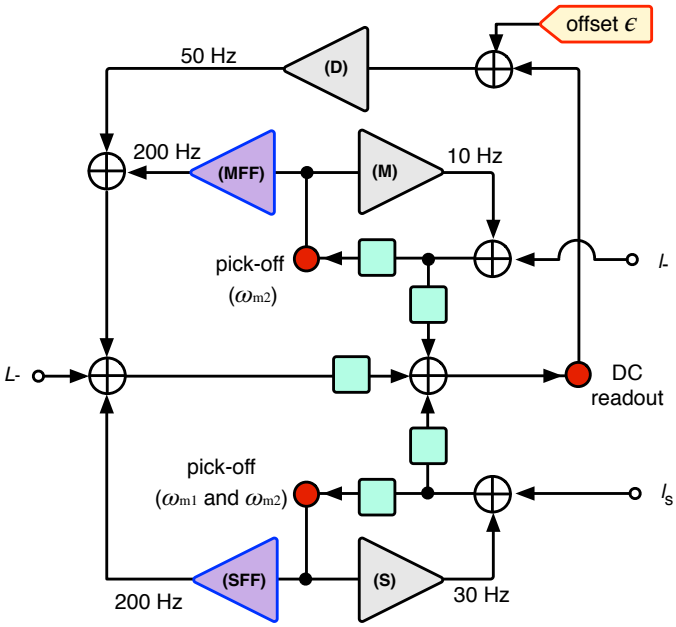

FIG. 4. A block diagram of the differential mode control network used in Advanced LIGO. A red disk represents a photodetector. A triangular block indicates a user-configurable control filter. A rectangular block represents a sensing coefficient which is in general a function of frequency. The annotations are as follows: (D) feedback control of the differential arm cavity length, L_-, using the DC readout signal, (M) feedback control of the Michelson length, l_-, using the ω_{m2} demodulation signal at the pick-off port, (MFF) feedforward filter for subtracting the coupling of the Michelson length into the differential arm cavity length, (S) feedback control of the signal recycling cavity, l_s, using a linear combination of the ω_{m1} and ω_{m2} demodulated signals from the pick-off port, and (SFF) feedforward filter for subtracting the coupling of the signal recycling cavity length into the differential arm cavity length.

simplified diagram of the differential control topology. The signal recycling cavity length is included here as well, since it has a rather large coupling coefficient into the differential arm cavity length. The power recycling cavity length is omitted, since its coupling is small and negligible. The main problem in controlling the differential mode lengths is to preserve the low noise readout for gravitational wave detection, rather than deriving robust signals.

The DC readout signal derived in Eq. (13) is sensitive to all auxiliary lengths. In particular, the Michelson length and the signal recycling cavity length are troubling. These degrees of freedom experience significantly more sensing noise than the antisymmetric port

signal—mainly due to the lower finesse and lower available light power. Even if they are controlled to a precision of better than a fraction of a nanometer rms, the residual displacement still contaminates the DC readout signal. Within the servo bandwidth, the shot noise of the auxiliary degrees of freedom is imprinted onto the motion of the auxiliary lengths. This will pollute the gravitational wave readout signal through the cross couplings—unless we implement two feedforward paths to directly subtract the noise from the differential arm cavity length.

In Advanced LIGO, the typical control bandwidth of the differential arm cavity servo is between 40 and 60 Hz. The Michelson length is derived from the quadrature phase signal at the pick-off port using ω_{m2} demodulation. In principle, one could use the reflection port or the other RF sideband pair, but this is the signal with the highest signal-to-noise. The contamination of the Michelson length by the differential arm cavity length is negligible.

Two feedforward control paths are implemented to subtract the noise from the Michelson length and from the signal recycling cavity length. The feedforward control for the Michelson length feeds the sensing signal to the differential arm cavity length, so that the combined actuator for the Michelson length does not produce a signal at the DC readout port. One can consider this method as the Michelson actuator diagonalization. Any remaining noise in the Michelson sensing will then have minimal coupling into the gravitational wave readout. The coupling from the signal recycling cavity controls can be suppressed with a similar feedforward path. In Advanced LIGO, the two feedforward paths successfully reject the noise from the auxiliary degrees of freedom in the frequency band from a few Hz to 200 Hz.

V. CONCLUSIONS

The dual recycled Fabry-Perot Michelson interferometer is the prevailing interferometer topology for building terrestrial gravitational wave antennae. In this configuration, the interferometric signals for sensing the individual length degrees of freedom are inevitably cross coupled because of the multiple optical resonators. A crucial feature is the ability of being able to design and implement a length control system, which is both robust and experiences low noise. We have analytically analyzed the length sensing and control scheme of Advanced LIGO. This scheme has been successfully implemented and lead to the first discovery of a black hole merger.

The analysis clearly shows the frequency dependent response and derives all relevant sensing signals at the antisymmetric port, in reflection and at the pick-off port of the detector. It analytically demonstrates the usefulness of the gain hierarchy approach for decoupling the common mode degrees of freedom. We also show how to robustly extract a signal for the signal recycling cavity length by linearly combining two different signals from the pick-off port.

For the gravitational wave readout at the antisymmetric port we demonstrate analytically that feedforward servos from the Michelson and signal recycling cavity degrees of freedom lead to a low noise readout. Radiation pressure plays an important role, since it couples the recycling cavities to the gravitational wave readout by physically displacing the mirrors in the Fabry-Perot arm cavities.

Summarizing, we have gained a thorough and comprehensive understanding of the complicated mechanics of a dual recycled Fabry-Perot Michelson interferometer, where multiple coupled optical resonators are interacting in subtle ways. This study serves as a starting point for designing future detectors, which will inevitably lead to many more astrophysical discoveries.

ACKNOWLEDGMENTS

The authors gratefully acknowledge K. Kawabe, S. Dwyer and E. Hall for fruitful discussions. LIGO was constructed by the California Institute of Technology and Massachusetts Institute of Technology with funding from the National Science Foundation and operates under cooperative agreement PHY-0757058. This paper has LIGO Document No. LIGO-P1500277.

APPENDIX: NUMERICAL PARAMETERS

Table I summarizes the optical and mechanical parameters used in this paper. For simplicity, none of the optics have losses.

symbol	description	value	units
$t_{\rm i}^2$	Input mirror power transmission	0.0140	
$r_{\rm i}^2$	Input mirror power reflectivity	0.986	
$r_{\rm e}^2$	End mirror power reflectivity	0.99995	
$t_{\rm p}^2$	Power recycling mirror power transmission	0.031	
$r_{\rm p}^2$	Power recycling mirror power reflectivity	0.969	
$t_{\rm s}^2$	Signal recycling mirror power transmission	0.35	
$r_{\rm s}^2$	Signal recycling mirror power reflectivity	0.65	
	Distances		
$L_{\rm x,y}$	Arm cavity length	3994.5	m
$l_{\rm sch}$	(Half of) Schnupp asymmetry	0.04	m
$l_{\rm p}$	Power recycling cavity length	57.65	m
$l_{\rm s}$	Signal recycling cavity length	56.0	m
$L_{\rm offset}$	Differential arm length offset	5×10^{-12}	m
	Laser properties		
$P_{\rm in}$	Input laser power	125	W
$\omega_{\rm m1}$	Modulation frequency of the $1^{\rm st}$ RF sideband	$2\pi \times 9099451$	rad/s
$\omega_{\rm m2}$	Modulation frequency of the $2^{\rm nd}$ RF sideband	$2\pi \times 45497255$	rad/s
Γ_1	Modulation depth of the $1^{\rm st}$ RF sideband	0.1	rad
Γ_2	Modulation depth of the $2^{\rm nd}$ RF sideband	0.1	rad
	Mechanical property		
$m_{\rm i,\,e}$	Mass of input and end mirrors	39.5	kg

TABLE I. Summary of the optical and mechanical parameters.

[1] B. P. Abbott *et al.* (LIGO Scientific Collaboration and Virgo Collaboration), Phys. Rev. Lett. **116**, 131103 (2016).

[2] F. Acernese *et al.* (Virgo Collaboration), Class. Quantum Grav. **32**, 024001 (2015).

[3] Y. Aso, Y. Michimura, K. Somiya, M. Ando, O. Miyakawa, T. Sekiguchi, D. Tatsumi, and H. Yamamoto (KAGRA Collaboration), Phys. Rev. D **88**, 043007 (2013).

[4] B. P. Abbott *et al.* (LIGO Scientific collaboration), Rept. Prog. Phys. **72**, 076901 (2009).

[5] T. Accadia *et al.* (VIRGO collaboration), JINST **7**, P03012 (2012).

[6] H. Grote (for the LIGO Scientific Collaboration), *Gravitational waves. Proceedings, 8th Edoardo Amaldi Conference, Amaldi 8, New York, USA, June 22-26, 2009*, Class. Quantum Grav. **27**, 084003 (2010).

[7] J. Aasi *et al.* (LIGO Scientific Collaboration), Class. Quantum Grav. **32**, 074001 (2015).

[8] B. P. Abbott *et al.* (LIGO Scientific Collaboration and Virgo Collaboration), Phys. Rev. Lett. **116**, 061102 (2016).

[9] R. W. P. Drever, in *The Detection of Gravitational Waves*, edited by D. G. Blair (Cambridge University Press, 1991) pp. 306–328.

[10] R. W. P. Drever *et al.*, in *Quantum Optics, Experimental Gravity, and Measurement Theory*, NATO ASI Series B, Vol. 94, edited by P. Meystre and M. O. Scully (Plenum Press, New York, 1983) pp. 503–514.

[11] R. Schilling, (unpublished).

[12] B. J. Meers, Phys. Rev. D **38**, 2317 (1988).

[13] J. Mizuno, K. A. Strain, P. G. Nelson, J. M. Chen, R. Schilling, A. Rüdiger, W. Winkler, and K. Danzmann, Phys. Lett. A **175**, 273 (1993).

[14] A. Staley *et al.*, Classical and Quantum Gravity **31**, 245010 (2014).

[15] P. Fritschel, R. Bork, G. González, N. Mavalvala, D. Ouimette, H. Rong, D. Sigg, and M. Zucker, Appl. Opt. **40**, 4988 (2001).

[16] R. Abbott, R. Adhikari, S. Ballmer, L. Barsotti, M. Evans, P. Fritschel, V. Frolov, and G. Mueller, *Advanced LIGO Length Sensing and Control Final Design*, Tech. Rep. T1000298-v2 (LIGO lab., 2010) https://dcc.ligo.org/LIGO-T1000298/public.

[17] S. Dwyer, D. Sigg, S. W. Ballmer, L. Barsotti, N. Mavalvala, and M. Evans, Phys. Rev. D **91**, 082001 (2015).

[18] S. Hild, S. Chelkowski, and A. Freise, arXiv:0810.0604 (2008), 0810.0604.

[19] W. M. Regehr, *Signal Extraction and Control for an Interferometric Gravitational Wave Detector*, Ph.D. thesis, California Institute of Technology (1995).

[20] D. V. Martynov *et al.*, Phys. Rev. D **93**, 112004 (2016).

[21] L. Schnupp, "Internal modulation schemes," presented at the European Collaboration Meeting on Interferometric Detection of Gravitational Wave, Sorrento, Italy, 1988.

[22] T. T. Fricke *et al.*, Classical and Quantum Gravity **29**, 065005 (2012).

[23] R. L. Ward *et al.*, Classical and Quantum Gravity **25**, 114030 (2008).

[24] R. W. P. Drever, J. L. Hall, F. V. Kowalski, J. Hough, G. M. Ford, A. J. Munley, and H. Ward, Applied Physics B **31**, 97 (1983).

[25] B. S. Sheard, M. B. Gray, C. M. Mow-Lowry, D. E. McClelland, and S. E. Whitcomb, Phys. Rev. A **69**, 051801 (2004).

[26] M. Evans *et al.*, Phys. Rev. Lett. **114**, 161102 (2015).

[27] M. Evans, *Optickle*, Tech. Rep. T070260-v1 (LIGO lab., 2007) `https://dcc.ligo.org/LIGO-T070260/public`.

[28] K. Somiya, Y. Chen, S. Kawamura, and N. Mio, Phys. Rev. D **73**, 122005 (2006).